Journal of Southeast University (English Edition) Vol. 42, No. 2, pp. 187-197 June 2026 ISSN 1003-7985

Application and performance evaluation of prestressed cable-stayed systems in large-scale offshore recovery towers

SUN Zhenlian[1], NIE Xinxin[2], WANG Ying[2]

(1. Beijing Institute of Aerospace Launch Technology, Beijing 100076, China; 2. Jiangsu Key Laboratory of Mechanical Analysis for Infrastructure and Advanced Equipment, Southeast University, Nanjing 211189, China)

Abstract: The offshore rocket recovery tower is an essential infrastructure for reusable space transportation. To address the lack of design methods and quantitative performance evaluation approaches for prestressed cable-stayed bracing systems under asymmetric and complex loading, this study develops an asymmetric two-stage prestressed cable-stayed bracing system for a large-scale offshore recovery tower with a height of 67 m and plan dimensions of 54 m × 70 m. Dual-platform finite element models were established in MIDAS Gen and SAP2000, and 292 full-condition load combinations were analyzed using a nonlinear step-by-step inheritance algorithm. In parallel, a refined Abaqus solid model was employed to verify the core load-bearing joint locally. Prestressing reduced the maximum *X*-direction deformation under transportation conditions from 263. 2 to 222. 1 mm, yielding safety margins of 14. 6% and 17. 5% in the *X*- and *Y*-directions, respectively. The stresses in the main structural members were markedly improved—the Q460 truss and beam elements satisfied the allowable-stress limits, whereas the Q355 truss elements remained only slightly above the limit. The local maximum von Mises stress at the inner pulley block joint reached 891. 9 MPa, indicating a risk of local yielding. These results demonstrate that the asymmetric prestressed cable-stayed bracing system can effectively enhance the global stiffness and force-transfer performance of large-scale offshore recovery towers, and that the full-process analytical framework established in this study provides a theoretical basis and engineering reference for the design and performance evaluation of analogous offshore aerospace support structures.

Key words: offshore rocket recovery tower; prestressed cable-stayed system; nonlinear step-by-step inheritance algorithm; mechanical performance evaluation; refined joint simulation

DOI: 10. 3969/j. issn. 1003-7985. 2026. 02. 005

Received 2026-03-05, **Revised** 2026-04-19.

Biographies: SUN Zhenlian (1987—), female, master, senior engineer; WANG Ying (corresponding author), female, doctor, professor, civil_wangying@seu. edu. cn.

Foundation item: The National Natural Science Foundation of China (No. 52578356).

Citation: SUN Zhenlian, NIE Xinxin, WANG Ying. Application and performance evaluation of prestressed cable-stayed systems in large-scale offshore recovery towers[J]. Journal of Southeast University (English Edition), 2026, 42(2): 187-197. DOI: 10. 3969/j. issn. 1003-7985. 2026. 02. 005.

Reusable launch vehicle technology is the critical pathway to achieving low-cost, high-frequency space transportation. Offshore vertical recovery has become an important development direction for reusable rocket recovery technology due to its advantages of flexible launch latitude, high landing zone safety, and wide mission adaptability[1]. Since SpaceX's Falcon 9 rocket successfully achieved offshore platform recovery, research on rocket recovery technology has advanced rapidly worldwide.

Existing studies have primarily focused on rocket airframe flight control and trajectory optimization, such as wind field disturbance estimation and attitude control during recovery[2], trajectory optimization and guidance algorithms for the powered descent phase[3-4], and buffer-capture mechanism design for heavy-load recovery[5-6]. Meanwhile, the structural response of offshore operating platforms has gradually attracted attention. Ashish et al.[7] conducted parametric studies on the structural response of deep-sea rocket launch platforms across multiple sea states, revealing the dynamic response laws of platforms under the coupled effects of wind, waves, and thrust. Pang et al.[8] analyzed the impact response characteristics of sea-based launch platforms through experiments and numerical simulations. Wang et al.[9] established a dynamic gap evaluation method between rockets and launch frames to address safety issues in sea-based rocket launches under extreme sea states. These studies provide important references for the design of infrastructure for offshore rocket recovery.

In ocean engineering, the prestressed cable-stayed system, a novel rigid-flexible coupling structural form, develops reverse pre-stiffness through the active tensioning of prestressed cables. It has been successfully applied across multiple fields because it can effectively optimize structural internal force distribution, enhance overall stiffness, and suppress structural deformation. In foundation engineering, Adegbulugbe et al.[10] investigated the impact response of prestressed concrete piles in marine environments, verifying that prestressing improves bearing capacity and corrosion resistance. Li et al.[11] theoretically predicted the corrosion life of loaded prestressed piles in marine environments, revealing how prestressing inhibits chloride-ion diffusion. In offshore wind power structures, Jin et al. [12] proposed prestressed concrete-filled double-skin steel tube columns suitable for offshore wind turbines, systematically analyzed their tension-compression hysteretic behavior, and verified that prestressing enhances component bearing capacity. Li et al. [13] conducted an optimization design for prestressed hybrid support structures of offshore wind turbines, reducing structural costs while improving overturning resistance. Zhou et al. [14] proposed a prestressed ultrahigh-performance concrete-steel hybrid tower for 15 MW offshore wind turbines, verifying its mechanical performance under extreme sea states. In long-span cross-sea bridges, Fang et al. [15] studied the wind-induced vibration control of cable-stayed bridges in strong marine wind environments and verified the vibration-suppression effect of cable-stayed systems. Recent studies have further extended the analysis of cable-stayed systems toward refined dynamic response and deformation control. Wang et al. [16] established analytical expressions for the vertical-bending and torsional modal frequencies of a two-cable-supported flexible photovoltaic bracket and revealed how the structural frequencies evolve with cable force, cable spacing, and sag effects, highlighting the important role of cable force regulation in the dynamic performance of cable-supported systems. Wang et al. [17] proposed a calculation method for the longitudinal end motion of long-span railway suspension bridges considering the longitudinal nonlinear resistance of stiffening girders, and showed that the cable-girder relative displacement and the forces in key connecting members are highly sensitive to nonlinear restraint conditions.

In summary, existing research has made significant progress in rocket airframe control, offshore platform dynamic response, and prestressing applications in conventional marine structures. However, clear research gaps remain for the special case of large-scale offshore rocket recovery towers. First, most studies focus on rocket flight control or the overall response of offshore platforms, whereas systematic investigations into the structural design and performance evaluation of dedicated large recovery towers that provide capture, buffering, and positioning support during recovery are still lacking. Second, most studies on prestressed cable-stayed systems address structures with symmetric layouts and regular loading. Traditional symmetric systems, which rely on uniformly distributed cables and unified tension-control strategies, cannot accommodate the asymmetric geometry and complex asymmetric loading of large offshore recovery towers. Accordingly, the design principles and force-transfer mechanisms of asymmetrically arranged two-stage prestressed cable-stayed bracing systems, as well as the quantitative effects of prestressing on the mechanical performance of such structures, remain to be clarified.

To address these research gaps and engineering demands, this study considers a large-scale offshore rocket recovery tower with a height of 67 m and a span of 54 m × 70 m. The structure adopts an asymmetrically arranged two-stage prestressed cable-stayed bracing system and represents a new steel structural system deployed in the offshore rocket recovery scenario. Unlike conventional land-based steel structures on fixed foundations, it must withstand the coupled effects of ship-motion-induced inertial forces during offshore transportation, rocket capture impact loads during operation, and multidirectional wind loads under extreme sea states, thereby imposing stringent requirements on stiffness, strength, and impact resistance. Dual-platform finite element models (FEMs) were established in MIDAS Gen and SAP2000, and a nonlinear step-by-step inheritance algorithm was used to accurately introduce the prestress field and to evaluate the stiffness, strength, and stability of the structure under 292 full-condition load combinations. On this basis, the inner pulley block, which is the core load-bearing joint along the structural load transfer path, was analyzed using a refined Abaqus solid model to determine its stress distribution, deformation characteristics, and plastic development. By integrating these procedures, this study establishes a full-process analytical framework comprising the dual-model verification of the global system, refined simulation of the key joint, and performance optimization, thereby enabling a multidimensional performance evaluation of large-scale offshore recovery towers from the overall system to the local joint scale. The resulting methodology provides a theoretical basis and engineering reference for the design and performance evaluation of analogous offshore aerospace support structures.

1 Engineering Overview and Research Methods

1.1 Structural system overview

The offshore rocket recovery tower investigated in this study is a prestressed cable-stayed mega steel frame designed for a real offshore rocket recovery mission and is therefore subject to explicit functional constraints. Its dimensions are governed jointly by the size of the recovery vessel, the requirements for rocket capture and buffering, and the net operating clearance within the tower, thereby satisfying the spatial demands of rocket passage, capture, and buffering operations while accommodating the height-positioning requirements of the recovery process. The main structure has a height of 67 m and plan dimensions of 54 m × 70 m. The primary load-bearing frame consists of a 54 m × 54 m upper cross beam, a 54 m × 70 m lower cross beam, and 67 m high inclined columns with an inclination angle of 4°. The main structure adopts a composite section comprising trusses and steel plate shear walls, together with 16 stay cables to form a spatially stable load-bearing system. These include eight 180 mm-diameter cables connected to the lower cross beam, four 180 mm-diameter cables connected to the structural supports, and four 120 mm-diameter restraint cables along the ship-length direction. The recovery tower system and cable arrangement are shown in Fig. 1.

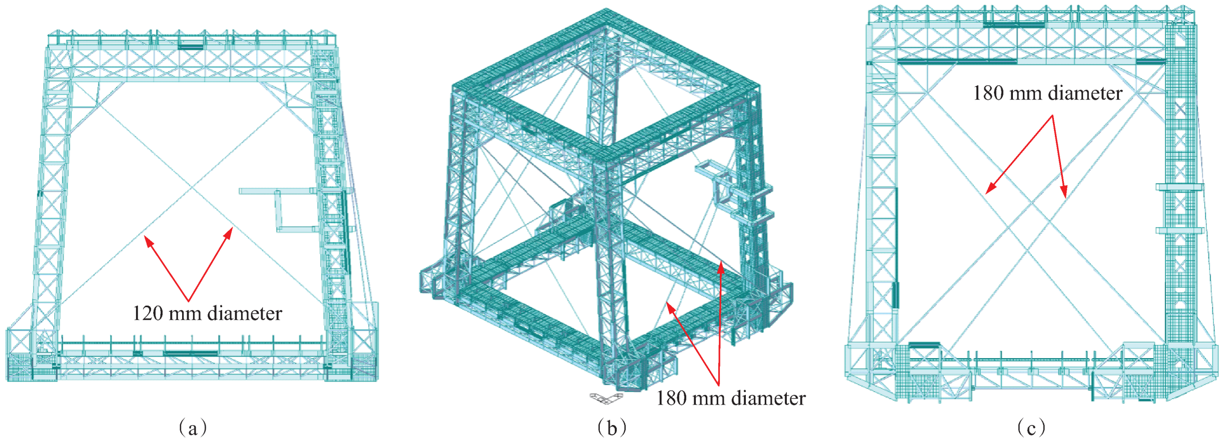

Fig. 1 Recovery tower system and cable arrangement. (a) Two 120 mm-diameter cables on the ship length side; (b) Two 180 mm-diameter cables connected to the lower cross beam on the ship width side; (c) Two 180 mm-diameter cables connected to the support on the ship width side

The stay cables adopt a two-stage prestressed tensioning control scheme, with design tension forces of 180 t for the 180 mm cables and 100 t for the 120 mm cables. Through active prestressing, the stay cables and steel frame form a rigid-flexible coupled load-bearing mechanism that enables the precise regulation of structural stiffness and internal force distribution and helps balance multidirectional stiffness requirements against impact resistance demands for a large-span tower on a floating offshore foundation. When the upper cross beam is subjected to a 1 075 kN vertical exhaust-flame impact load, the load is transferred to the inclined columns through the double-layer truss, and lateral restraint is provided by the paired cables along the ship-width direction. Under the 750 kN capture load on the lower cross beam, the cantilevered steel plate shear walls act together with the single-layer truss, while the stay-cable tension directly balances the horizontal load. The 4° inclined columns optimize the transfer paths of vertical and horizontal loads, enabling asymmetric loads to be transmitted efficiently to the foundation through a cable-column axial force path and substantially reducing the bending-moment demand in the structural members.

1. 2 Design criteria and load cases

The tower structure has a design safety level of Grade Ⅰ and a design service life of 20 years. The design and analysis strictly follow the current national codes, including the GB 50068—2018 Unified Standard for Reliability Design of Building Structures, the GB 50017—2017 Standard for Design of Steel Structures, and the JGJ 257—2012 Technical Specification for Cable Structures.

This study evaluates the main members using the allowable-stress method. In accordance with the project-specific safety requirements, the allowable-stress limits were determined from the steel yield strength using a safety factor of 2. 0. These limits implicitly account for stability effects: the main structure is a mega-truss system with relatively short effective lengths of the beam-column members, resulting in relatively large stability coefficients. Additional stability checks were performed for the key controlling members to ensure that their stability stresses meet the code requirements.

The main structure is fabricated from Q355 and Q460 steels, with allowable stresses of 240 and 310 MPa, respectively. Considering the full-service lifecycle of the tower, the coupled effects of dead load, prestress, wind load, sea-state-induced inertial forces, rocket exhaust-flame impact load, capture load, and buffer load were considered. Sea States 4 (transverse 0. 50g, longitudinal 0. 20g, vertical 0. 30g), 5 (0. 90g, 0. 35g, 0. 45g), and 7 (1. 50g, 0. 45g, 0. 45g) were converted into 32 inertial force combinations, and a mass-to-nodal-load dynamic conversion method was used to apply the 132 t buffer load. These sea states were selected based on measured marine environmental parameters in waters commonly used for offshore rocket launch and recovery in China, together with full-process safety control requirements for reusable rocket offshore recovery missions. Sea State 4 corresponds to the maximum operating sea state for rocket recovery operations, Sea State 5 to the maximum sea state during offshore transportation, and Sea State 7 to the extreme survival sea state over the full lifecycle, thereby covering the key loading scenarios from transportation and operation to extreme survival.

The exhaust-flame impact load was increased by 0-17% relative to the theoretically calculated resultant force to account for load uncertainty and safety margins, and was applied as nodal loads at the corresponding locations.

Load combinations followed a three-level control strategy. The fundamental combination was used for strength checks, with partial factors of 1.3 for dead load, 1.5 for capture and service loads, and 1.5 for wind load. The characteristic combination was used for stiffness checks, with a partial factor of 1.0 for all permanent and variable loads and 0.6 for wind load. The special combination was used for transportation conditions, superimposed with stabilizing wire-rope loads, with a partial factor of 1.0. On this basis, the loading process was divided into five operational stages—parking, transportation, pre-capture, capture, and post-capture—which were further subdivided into ten calculation categories. Except for the parking condition, the remaining nine categories each considered four wind directions and eight inertial force directions, giving $4 \times 8 = 32$ load combinations per category; the parking condition considered only four wind directions. Accordingly, the nonlinear step-by-step analysis included a total of $4 + 9 \times 32 = 292$ load combinations. The stiffness criteria were defined as a maximum global deformation of 260 mm under transportation conditions and a maximum mid-span relative deformation of 44 mm for the upper cross beam. The strength criterion was that member stresses should not exceed the corresponding allowable-stress limits.

1.3 Finite element model construction and verification

1.3.1 Dual-platform finite element model construction

Structural design and independent verification models were established in MIDAS Gen and SAP2000, respectively, for dual-platform cross-validation. The elastic modulus of both Q355 and Q460 steels was taken as 206 GPa, with a Poisson's ratio of 0.3, whereas the prestressed stay cables were assigned an elastic modulus of 190 GPa and a Poisson's ratio of 0.3. Truss members and beam-column members were represented by beam elements; joints were treated as rigid, with end bending restraints retained to allow full transmission of the axial force, shear force, and bending moment. Steel plate shear walls and node plates were modeled using shell elements. The prestressed stay cables were represented by tension-only cable elements with end bending restraints released, and prestress was introduced through the initial cable force. The boundary conditions were defined as fixed supports at the base to represent the welded rigid connection between the tower and the offshore operating platform and thus capture their cooperative load-bearing behavior.

In wind load calculation, a wind shielding coefficient reflecting the structural ventilation characteristics is introduced and dynamically adjusted according to the actual structural configuration and wind direction at different parts of the structure to achieve an accurate simulation of wind loads.

1.3.2 Nonlinear step-by-step inheritance algorithm

To capture the pronounced geometric nonlinearity of the cable-stayed system and the time-dependent loading sequence, a nonlinear step-by-step inheritance algorithm was adopted (Fig. 2) for the refined simulation of prestress introduction and multi-condition loading. The calculation process is as follows:

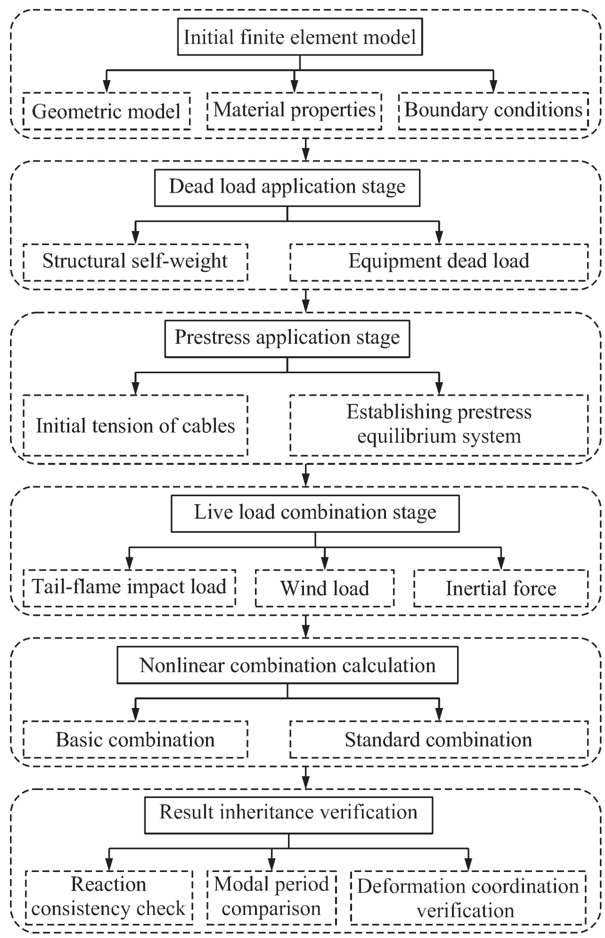

Fig. 2 Technical flowchart of the nonlinear combination and step-by-step inheritance algorithm

An initial FEM incorporating geometry, material properties, and boundary conditions was first established, after which self-weight and equipment dead loads were applied to obtain the baseline stress state. Prestress was then introduced using a two-stage tensioning scheme, with design tension forces of 180 t for the 180 mm-diameter cables and 100 t for the 120 mm-diameter cables. In the MIDAS Gen model, the initial cable forces were adjusted manually through iterative tuning to achieve accurate prestress application, whereas in the SAP2000 model, prestress was introduced using a target-force iteration procedure to establish the prestressed equilibrium state that served as the initial stress condition for subsequent live-load analysis. In the live-load stage, variable actions, including exhaust-flame impact, wind load, and inertial forces, were combined using the fundamental and characteristic combinations for strength and stiffness evaluation, respectively. For the 292 load combinations, a multi-step nonlinear analysis sequence was further established to capture nonlinear accumulation through stiffness-matrix inheritance. Taking a representative capture condition as an example, a three-stage loading sequence was adopted: Stage 1 applied 1.3 times the dead load to establish the initial stress field; Stage 2 introduced 1.0 times the buffer load and exhaust-flame impact load; and Stage 3 superimposed 1.5 times the wind load and multidirectional inertial force combinations.

During the calculation process, the consistency of load transfer paths is strictly maintained. Through cross-comparison of the calculation results from the two platforms, it is verified that the model satisfies the requirements of relevant codes in terms of reaction force balance, modal characteristics, and deformation coordination.

1.3.3 Dual-model consistency verification

To ensure the reliability of the FEMs and the accuracy of the calculation results, consistency verification was conducted between the MIDAS Gen design model and the SAP2000 recalculation model from two dimensions: base reaction forces and dynamic characteristics.

The comparison results of the total base reaction forces of the two models under dead load and each single load case are presented in Table 1. The results show that the error of the Z-direction reaction force under dead load conditions is less than 0.1%, and the difference in inertial force loads is controlled within 2%. Under wind load, buffer load, capture load, exhaust-flame impact load, and other conditions, the total base reaction forces of the two models are completely consistent, verifying the accuracy of the model geometry, boundary conditions, and load application.

Eigenvalue modal analysis was performed on both models. The results show that the first five mode shapes of the structure are consistent. The comparison of the first-order mode shapes is shown in Fig. 3. The first-order modal periods are 1.042 8 (MIDAS Gen) and 1.024 2 s (SAP2000), with a period deviation of only 1.8%. The period deviations of the first five modes are all within 3%, and the dynamic characteristic matching degree of the structure reaches more than 97%, further verifying the rationality and reliability of the FEMs.

Table 1 Comparison of total base reaction forces of dual models under different load cases

Load case	Total base reaction force/MN		Relative deviation/%
	MIDAS design model	SAP2000 recalculation model	
Dead load Z-direction force (self-weight)	38.860 0	38.885 8	<0.1
Dead load Z-direction force (auxiliary equipment)	14.125 4	14.125 4	0
X-direction wind load (transportation)	3.754 7	3.754 7	0
Y-direction wind load (transportation)	3.869 8	3.861 7	<0.2
X-direction wind load (service)	2.188 1	2.188 1	0
Y-direction wind load (service)	2.231 9	2.227 1	<0.2
Buffer load Z-direction force	7.840 0	7.840 0	0
Capture load Z-direction force	5.280 0	5.280 0	0
Upper cross beam exhaust-flame impact Z-direction force	5.680 0	5.680 0	0
Lower cross beam exhaust-flame impact Z-direction force	4.048 0	4.048 0	0
0.90g X-direction inertial force	47.591 7	48.451 1	1.8
0.35g Y-direction inertial force	18.507 9	18.842 1	1.8
0.45g Z-direction inertial force	23.795 9	24.225 6	1.8

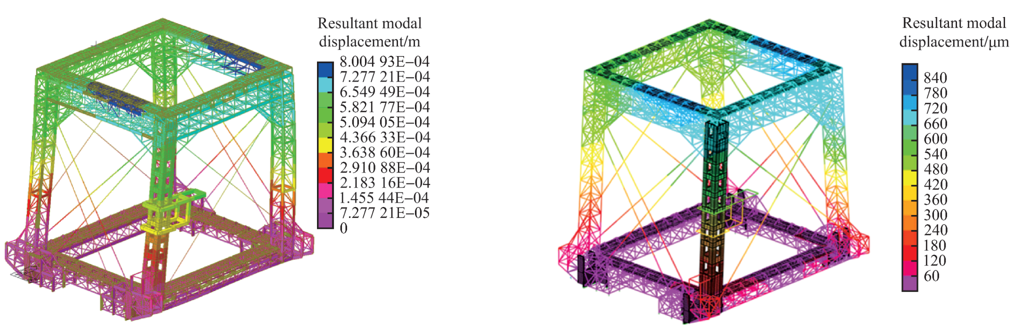

(a) (b)

Fig. 3 Comparison of first-order mode shapes. (a) MIDAS design model; (b) SAP2000 recalculation model

2 Mechanical Performance Analysis of the Overall Structure

2.1 Stiffness performance evaluation

The stiffness enhancement effect of the prestressed cable-stayed system was evaluated, and the stiffness service reliability of the structure under extreme conditions was verified, taking the overall deformation limit under transportation conditions and the mid-span relative deformation limit of the upper cross beam as the core stiffness control indicators.

2.1.1 Deformation control under transportation conditions

The transportation condition combining Sea State 5 (0.90g transverse inertial force) and Grade 10 wind load (0.50 kN/m^2) is the control condition for the overall deformation of the structure. The deformation contours and numerical comparisons of the structure with and without prestress are shown in Fig. 4 and Table 2, respectively.

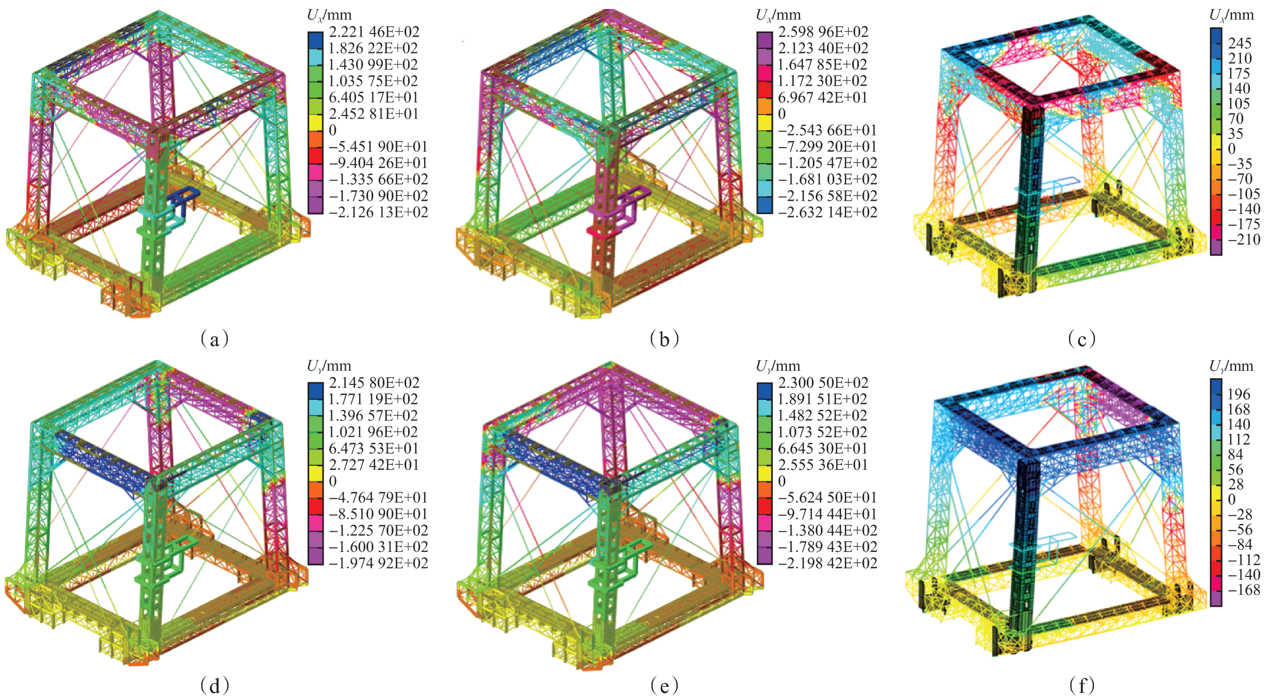

Fig. 4 Structural deformation contours under different transportation conditions. (a) MIDAS model with prestress (*X*-direction); (b) MIDAS model with prestress (*Y*-direction); (c) MIDAS model without prestress (*X*-direction); (d) MIDAS model without prestress (*Y*-direction); (e) SAP2000 model with prestress (*X*-direction); (f) SAP2000 model with prestress (*Y*-direction)

Table 2 Comparison of structural deformations with and without prestress under different transportation conditions mm

Direction	Deformation			Deformation limit
	MIDAS model without prestress	MIDAS model with prestress	SAP2000 model with prestress	
X-direction	263.2	222.1	227.6	260
Y-direction	230.0	214.6	215.3	260

The results show that, without prestress, the maximum *X*-direction deformation reached 263.2 mm, exceeding the 260 mm code limit and indicating insufficient stiffness. After prestressing, the maximum deformations in the *X*- and *Y*-directions decreased to 222.1 (MIDAS) and 227.6 mm (SAP2000), and to 214.6 (MIDAS) and 215.3 mm (SAP2000), respectively, all satisfying the deformation limit. The corresponding safety margins were 14.6% in the *X*-direction and 17.5% in the *Y*-direction. The dual-model comparison confirms that prestressing markedly reduces global deformation and enhances overall stiffness. Mechanistically, active cable tensioning induces an upward force in the main steel frame opposite to the external lateral loading, thereby generating reverse pre-stiffness that directly counteracts the lateral actions arising under transportation and recovery conditions. Concurrently, the system transforms the unfavorable bending-dominated load path of the original frame into an efficient axial force transfer mode, with the cables primarily in tension and the inclined columns primarily in compression. This substantially reduces the bending moments in the beams and columns, redistributes internal forces throughout the structure, and transfers loads away from the original high-stress regions toward the cables and columns, thereby reducing overall deformation while improving the stress distribution of the main members.

2.1.2 Relative deformation control of the upper cross beam

As the core support component for rocket recovery operations, the mid-span relative deformation of the upper cross beam directly affects the positioning accuracy and operational safety during recovery, with a design limit of 44 mm. The deformation results of the upper cross beam calculated by the dual models under the pre-capture condition are shown in Fig. 5.

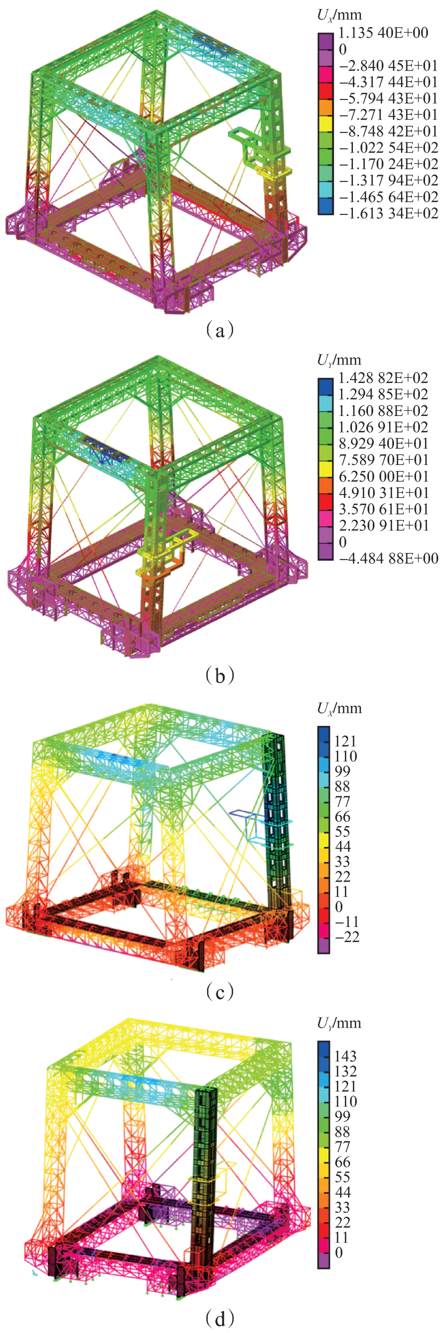

Fig. 5 Deformation diagrams of the upper cross beam under pre-capture conditions. (a) MIDAS model with prestress (*X*-direction); (b) MIDAS model with prestress (*Y*-direction); (c) SAP2000 model with prestress (*X*-direction); (d) SAP2000 model with prestress (*Y*-direction)

The calculation results of the MIDAS model show that, under the pre-capture condition, the mid-span deformation of the upper cross beam in the *X*-direction is 161.1 mm, the deformations at both ends are 113.4 and 123.1 mm, and the mid-span relative deformation is 42.85 mm. The mid-span deformation in the *Y*-direction is 142.9 mm, the deformations at both ends are 101.5 and 101.2 mm, and the mid-span relative deformation is 41.55 mm. The calculation results of the SAP2000 model show that, under the pre-capture condition, the mid-span deformation of the upper cross beam in the *X*-direction is 110.7 mm, the deformations at both ends are 83.2 and 65.3 mm, and the mid-span relative deformation is 36.45 mm. Conversely, the mid-span deformation in the *Y*-direction is 128.1 mm, the deformations at both ends are 80.0 and 90.1 mm, and the mid-span relative deformation is 43.05 mm. The specific values of the mid-span relative deformation of the upper cross beam are presented in Table 3.

Table 3 Deformation stiffness of the upper cross beam

mm

Direction	Deformation		Deformation limit
	MIDAS model	SAP2000 model	
X-direction	42.85	36.45	44
Y-direction	41.55	43.05	44

The results show that the mid-span relative deformation of the upper cross beam obtained from both models does not exceed the limit of 44 mm, thus satisfying the stiffness design requirements. Among them, the *X*-direction mid-span relative deformation predicted by the SAP2000 model is approximately 15% lower than that obtained from the MIDAS model. Although the *Y*-direction result is close to the limit, it still satisfies the design requirement. This difference is mainly attributed to the differences between the two software packages in element treatment and nonlinear solution strategies. Despite the numerical deviations, the results of both models satisfy the design limits, thereby confirming the effective control exerted by the prestressed cable-stayed bracing system on the deformation of the upper cross beam. Moreover, the reliability of the models has been cross-validated through key indicators such as base reactions and modal periods.

2.2 Strength performance evaluation

2.2.1 Stress distribution of main components

The maximum stresses of the main members with and without prestress are summarized in Table 4. For the truss elements, the reported stress denotes the axial stress along the member axis, whereas for the beam elements, it denotes the combined stress under the coupled action of axial force and biaxial bending moments. These stresses were obtained from the global FEM and evaluated in accordance with the Standard for the Design of Steel Structures. Without prestress, the maximum stresses in the Q355 and Q460 truss elements were 251.7 and 311.3 MPa, respectively, both exceeding the corresponding allowable-stress limits. After prestressing, these values correspondingly decreased to 244.5 and 296.8 MPa. The Q460 truss elements thus satisfied the allowable-stress limit of 310 MPa, whereas the Q355 truss elements remained slightly above the 240 MPa limit, by approximately 1.9%. The beam elements exhibited a similar trend. The maximum stress of the Q355 beam elements decreased from 253.0 to 239.0 MPa, thereby satisfying the design limit, while that of the Q460 beam elements decreased from 311.5 to 306.5 MPa, below the allowable-stress limit of 310 MPa.

Table 4 Comparison of maximum stresses of main components MPa

Component type	Maximum stress		Allowable stress limit
	Design model with prestress	Design model without prestress	
Q355 truss element	244.5	251.7	240
Q460 truss element	296.8	311.3	310
Q355 beam element	239.0	253.0	240
Q460 beam element	306.5	311.5	310
Q355 plate element	723.1	662.1	240
Q460 plate element	672.6	693.9	310

Prestressing introduces pre-bending moments in the frame beams and columns opposite to those induced by the service loads, thereby offsetting part of the bending-moment peaks under extreme conditions. More importantly, the prestressed system changes the unfavorable bending-dominated force-transfer mode into an efficient mode characterized by cable tension, column axial compression, and only small residual bending moments. This fundamental redistribution of internal forces lowers the maximum stress level of the main members.

2.2.2 Local stress concentration analysis

The calculations indicate pronounced stress concentration in the structural plate elements. The local maximum stress of the Q355 plate elements reached 723.1 MPa, whereas that of the Q460 plate elements reached 693.9 MPa, both far exceeding the corresponding allowable-stress limits. This local stress increase is primarily associated with local regions such as the cable-end anchorage plates and beam-column transition joints. Prestress introduces additional local internal forces at these locations, thereby increasing the local stress level. In addition, the plate element stresses obtained from the global beam-shell model inevitably contain numerical distortion, because the global model cannot accurately resolve the detailed stress distribution in the joints. These local stress concentrations were therefore re-examined by subsequent refined solid element analysis. Because the affected zones are highly localized, they do not compromise the global mechanical performance of the structure. The high-stress regions are concentrated near connections, section transitions, and support zones, reflecting local stress concentrations caused by the geometric complexity of the joints.

The overall bar-shell model cannot accurately capture the stress distribution and plasticity evolution of detailed joint structures. Therefore, refined numerical simulation using solid elements is required to clarify the real force-bearing state of core joints, evaluate their service safety, and propose targeted optimization and reinforcement measures.

3 Refined Numerical Simulation of the Inner Pulley Block Key Joint

The inner pulley block (fixed pulley joint of the lower stable buffer circuit) is the core force-bearing joint on the load transfer path of the tower structure. It directly bears the vertical tension and horizontal resultant force of the steel wire ropes, and is the key force-bearing component under extreme conditions such as buffering and capture. Its mechanical performance significantly affects the service safety of the overall structure. Aiming at the stress concentration problem in the joint area of the overall model, this section establishes a refined solid element model using Abaqus to conduct joint mechanical performance analysis and safety verification.

3.1 Construction of refined FEM for the joint

Based on the actual joint geometry, a 1∶1 refined solid model was established to reproduce the detailed configurations of the fixed pulley seat, connecting plates and stiffeners. The position of the joint in the overall structure and the solid model are shown in Fig. 6. The material parameters were kept consistent with those of the global model. Q690 high-strength steel was represented using an ideal elastic-plastic constitutive law, with an elastic modulus of 210 GPa and a Poisson's ratio of 0.3. The purpose of adopting the ideal elastic-plastic model was to determine whether the joint yields under the design load and thereby reveal potential safety hazards.

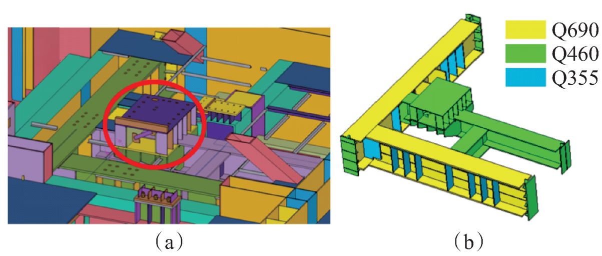

Fig. 6 Schematic diagram of the inner pulley block key joint. (a) Position of the fixed pulley joint in the overall structure; (b) Solid model of the joint

The control loads of the joint are taken from the results of the most unfavorable load case combination in the overall structural analysis: the fixed pulley seat is subjected to a vertical single-rope tension of 18.75 t and a horizontal rope resultant force of 65 t. The load is applied using the multi-point constraint method, which uniformly applies the concentrated load to the acting surface of the pulley seat through a reference point, ensuring that the load transfer mode is consistent with the actual force-bearing state. The boundary conditions adopt fixed constraints on the connection end faces between the joint and the main truss according to the actual constraint form of the joint in the overall structure, restoring the real boundary state of the joint. The mesh generation adopts a hybrid element scheme dominated by hexahedral elements and supplemented by tetrahedral elements. The mesh is refined in stress concentration areas such as the pulley seat and connecting plates, and the overall mesh size is controlled between 20 and 100 mm. The reference point setting, boundary condition setting, and mesh generation of the inner pulley block key joint are shown in Fig. 7.

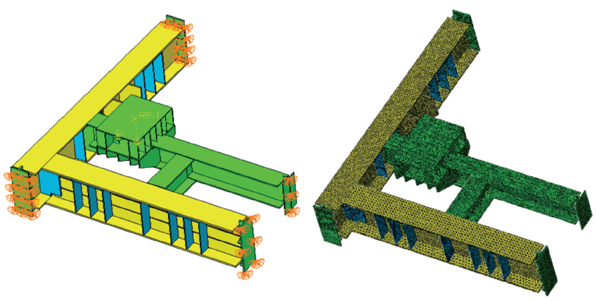

Fig. 7 Reference point setting, boundary condition setting, and mesh generation of the inner pulley block key joint. (a) Reference point and boundary condition settings; (b) Mesh generation

3.2 Analysis of joint mechanical performance results

The finite element results for von Mises stress, displacement, and equivalent plastic strain are shown in Fig. 8. For the present solid model, yielding was evaluated using the von Mises criterion; accordingly, the term "stress" in this subsection refers to von Mises equivalent stress under a multiaxial stress state. The stress distribution shows pronounced concentration at the intersection between the pin hole of the pulley seat and the connecting plate, where the local maximum von Mises stress reaches 891.9 MPa. This value represents a local numerical peak within the mesh-refined zone and does not indicate the stress state over a large material volume. Instead, it demonstrates severe local stress concentration, with the local region exceeding the 690 MPa yield strength of Q690 steel. Outside the local hotspot, most areas of the joint remain below 690 MPa, indicating that plastic development is limited in extent and manifests mainly as local yielding. The deformation field is relatively smooth, with a maximum displacement of 2.54 mm occurring at the load application point on the pulley seat, suggesting that the overall joint stiffness satisfies the service requirements and will not significantly impair the global structural deformation or the operating state of the steel wire ropes. The plastic strain distribution is broadly consistent with the stress field. The maximum equivalent plastic strain is 4.824×10^{-3} for the joint as a whole and 6.138×10^{-3} in the local high-stress region, further confirming local plastic yielding and the need for targeted reinforcement.

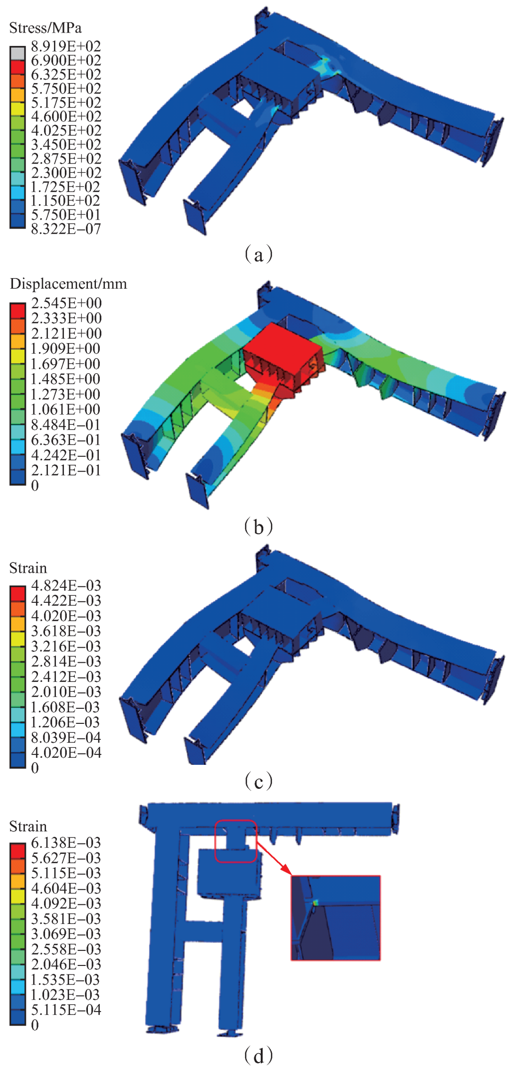

Fig. 8 Finite element calculation results. (a) Stress distribution; (b) Displacement distribution; (c) Plastic strain of the overall structure; (d) Plastic strain of the local structure

4 Conclusions

Using a large-scale offshore rocket recovery tower with a height of 67 m and a span of 54 m × 70 m as the case study, this study developed an asymmetric two-stage prestressed cable-stayed bracing system and conducted global structural analysis and key joint verification for 292 load cases using dual-platform FEMs and a nonlinear step-by-step inheritance algorithm. The main conclusions are as follows:

(1) The asymmetric two-stage prestressed cable-stayed bracing system markedly improves the global stiffness of the structure. Under the transportation control condition, combining Sea State 5 and Grade 10 wind load, the *X*-direction deformation of the structure without prestress exceeded the allowable limit. After prestressing, the maximum *X*- and *Y*-direction deformations were reduced to 222.1 and 214.6 mm, respectively, both satisfying the 260 mm limit and providing safety margins of 14.6% and 17.5%, respectively. Prestressed cables generate reverse pre-stiffness and reconstruct the internal force-transfer path, thereby enabling rigid-flexible cooperative action between the stay cables and the steel frame.

(2) The prestressed system substantially improves the force state of the main structural members. After prestressing, the maximum stresses of the Q355 and Q460 truss elements decreased to 244.5 and 296.8 MPa, respectively, whereas those of the Q355 and Q460 beam elements decreased to 239.0 and 306.5 MPa, respectively. Accordingly, the Q460 truss and beam elements satisfy the allowable-stress limits, while the Q355 truss elements are significantly improved but remain slightly above the limit, indicating that further adjustment through cable force optimization and local reinforcement is still required.

(3) The global and refined models together reveal the law of local stress concentration in the structure. Connections, section-transition zones, and regions adjacent to the supports are the principal high-stress areas in the beam-shell model. The refined solid analysis further shows that, under the most unfavorable load combination, the inner pulley block joint reaches a local maximum von Mises stress of 891.9 MPa and a maximum equivalent plastic strain of 6.138×10^{-3}, indicating a risk of local yielding.

(4) The dual-platform nonlinear step-by-step inheritance procedure adopted in this study can effectively capture the nonlinear cumulative effects of this class of rigid-flexible coupled structures under multiple loading scenarios. Cross-validation shows that the discrepancy in base reactions between the two models is less than 0.1% and that the deviations in the first five modal periods are within 3%, demonstrating that the method is suitable for the design analysis and performance assessment of analogous offshore aerospace support structures.

References

[1] DE ZAIACOMO G, BLANCO ARNAO G, BUNT R, et al. Mission engineering for the RETALT VTVL launcher[J]. CEAS Space Journal, 2022, 14(3): 533-549.

[2] FAN C X, HE W, ZHAO Y, et al. Adaptive load optimization and precision control scheme for vertical landing rockets with sparse sensing data[J]. Aerospace, 2026, 13(3): 255.

[3] YOU G Y, YANG M M. A two-stage successive convexification method for the powered descent guidance problem[J]. Scientia Sinica Mathematica, 2020, 50(9): 1361.

[4] ZHAO Y, LI C, YU Y N, et al. Review of rocket return and landing guidance methods[J]. Electronics Optics & Control, 2025, 32(2): 45-53. (in Chinese)

[5] XU D L, GUO S, XU X L, et al. Design and analysis of a delta-type rocket recovery mechanism based on an annular cushioning moving platform[J]. Journal of Mechanical Engineering, 2025, 61(21): 168-178. (in Chinese)

[6] ZHANG H, ZHANG C, SONG X D. Design and analysis of buffer device of cable system for reusable rocket recovery and landing[J]. Journal of Astronautics, 2022, 43(9): 1152-1162. (in Chinese)

[7] ASHISH P U, CHANDRASEKARAN S, SERINO G. Parametric study on the deep ocean space-rocket launching triceratops[J]. Ocean Engineering, 2024, 295: 116946.

[8] PANG F Z, QIN Y X, TANG Y, et al. Experimental study on impact response of seaborne rocket launch platform[J]. Ocean Engineering, 2023, 280: 114623.

[9] WANG D, SHAO J S, CAO N, et al. Safety assessment of framed hot launch departure for sea-based rockets in rough sea conditions[J]. Defence Technology, 2025, 50: 83-100.

[10] ADEGBULUGBE O, JUNG S, KAMPMANN R. Impact behavior of prestressed concrete piles with glass FRP spirals: Experimental and finite-element analysis[J]. Journal of Composites for Construction, 2024, 28(5): 04024049.

[11] LI L, YANG C Y, LI J P. Corrosion initiation life of laterally loaded PHC pipe piles served in marine environment: Theoretical prediction and analysis[J]. Construction and Building Materials, 2021, 293: 123457.

[12] JIN K Y, ZHOU X H, HU C, et al. Tensile-compressive hysteresis performance of prestressed CFDST columns for offshore wind turbine structures[J]. Ocean Engineering, 2026, 344: 123464.

[13] LI Z Y, XU B, YUAN G K. Optimization for offshore prestressed concrete-steel hybrid wind turbine support structure with pile foundation using a parallel modified particle swarm algorithm[J]. Journal of Marine Science and Engineering, 2024, 12(5): 826.

[14] ZHOU Z, ZHOU X H. Mechanical behavior of prestressed UHPC wind turbine tower columns under combined axial compression and bending[J]. Structural Concrete, 2025, 26(1): 465-480.

[15] FANG Z, ZHU Y. Analysis of wind-induced effects and vibration control of a cable-supported bridge with a steel truss girder in strong marine wind environments[J]. Applied Sciencess, 2025, 15(22): 11950.

［16］ WANG P X, FANG G S, GE Y J. Practical estimation formulas and evolution law for natural frequencies of two-cable-supported flexible photovoltaic supports［J/OL］. Journal of Southeast University（Natural Science Edition）, 2026［2026-02-05］. https://link. cnki. net/urlid/32. 1178. N. 20260205. 1458. 004.（in Chinese）

［17］ WANG H, LIU G, SHEN R L. Calculation method for girder-end longitudinal movement of long-span railway suspension bridges under train loads［J/OL］. Journal of Southeast University（Natural Science Edition）, 2026［2026-02-02］. https://link. cnki. net/urlid/32. 1178. N. 20260202. 1147. 002. （in Chinese）

预应力索撑体系在大型海上回收塔架中的应用与性能评估

孙振莲[1], 聂鑫鑫[2], 王莹[2]

（1.北京航天发射技术研究所,北京 100076;2.东南大学江苏省基础设施与先进装备力学分析重点实验室,南京 211189）

摘要: 海上火箭回收塔架是可重复使用航天运输的重要基础设施。针对现有研究缺乏面向非对称复杂受力特征的预应力索撑体系设计方法及量化性能评估方法的问题,以高67 m、跨度54 m × 70 m的大型海上回收塔架为对象,构建了非对称两级预应力索撑协同体系。基于MIDAS Gen与SAP2000建立双平台有限元模型,并结合非线性分步继承算法,完成292种全工况组合分析;同时针对核心受力节点,采用Abaqus建立实体精细化模型开展局部复核。结果表明:施加预应力后,运输工况下结构X向最大变形由263. 2 mm降至222. 1 mm,X向与Y向安全裕度分别达到14. 6%和17. 5%;主体构件应力整体得到明显改善,其中Q460桁架单元及梁单元满足容许应力限值,Q355桁架单元仅略超限;内滑轮组节点局部最大von Mises应力为891. 9 MPa,存在局部屈服风险。研究结果表明,非对称预应力索撑体系可有效改善大型海上回收塔架的整体刚度与受力性能,所建立的全流程分析方法可为同类海上航天支撑结构的设计与性能评估提供理论依据与工程参考。

关键词:海上火箭回收塔架;预应力索撑体系;非线性分步继承算法;力学性能评估;节点精细化模拟

中图分类号:TU394